https://doi.org/10.1016/j.desal.2024.118033

Highlights

Elucidating the use of pressure-recovery diagrams for analyzing energy consumption in reverse osmosis desalination

Mingheng Li, Shihong Lin

- Elucidated P-Y diagrams under constant design flux for analyzing SEC in RO
- Related minimal SEC imposed by design flux to equipartition of entropy production theorem
- Constructed P-Y diagrams for SWRO and BWRO and showed their differences
- Applied P-Y diagrams to compare the energy performance of CCRO, BRO and multistage RO
- Studied the effect of ultrapermeable membranes on the energy performance of SWRO and BWRO

Elucidating the use of pressure-recovery diagrams for analyzing energy consumption in reverse osmosis desalination

Mingheng Li^{a,*}, Shihong Lin^b

^aDepartment of Chemical and Materials Engineering, California State Polytechnic University, Pomona, CA 91768 USA ^bDepartment of Civil and Environmental Engineering, Vanderbilt University, Nashville, TN 37235-1831, USA

Abstract

The pressure-recovery (P-Y) diagram used in reverse osmosis (RO) literature to compare energy consumptions in different RO configurations has a flaw of not holding the design flux constant. In this work, the P-Y diagrams are constructed with the aid of transport models. It is shown that the area underneath the P-Y curve represents the specific energy consumption (SEC) imposed by design flux and thermodynamics, which may be reduced by improving spatial uniformity in flux. The trend generally observes the equipartition of entropy production theorem. For seawater RO (SWRO) in which pressure drop relative to feed osmotic pressure is small and operation is near the thermodynamic limit, staged designs with interstage booster pumps enable a more uniform flux, thus reducing the SEC. However, for low-salinity brackish water RO (BWRO), improving flux uniformity may lead to a higher SEC as the increased friction loss often outweighs the reduced energy requirement imposed by system flux.

Keywords:

pressure-recovery (P-Y) diagram, specific energy consumption (SEC), equipartition of entropy production, staged operation

^{*}Corresponding author. Tel: 909-869-3668. E-mail: minghengli@cpp.edu

1. Introduction

Diagrams such as pressure-volume (P-V) and temperature-entropy (T-S) are widely used in thermodynamic cycles [1]. The main advantages of these diagrams include a clear visualization of energy transfer in each step of a cycle and a direct comparison of energy efficiencies between two different cycles. For example, the area underneath the P-V curve in one cycle step describes the work done by the system, positive if the path is directed to the right. When the curve on the P-V diagram forms a closed shape, the net work done by the system is represented by the area enclosed by the cycle, positive if it is traversed clockwise. A larger enclosed area with the same heat input suggests a higher thermal efficiency.

In the RO desalination community, pressure-recovery (P-Y) diagrams have been frequently used as a graphical representation of energy consumption in RO as well as the energy saving of a new design relative to a baseline case [2, 3, 4, 5, 6, 7, 8]. One such example is shown in Figure 1. The blue and red solid lines show the applied pressures in the one-stage (RO-1) and multistage (RO-2 and RO-3) configurations, respectively. The dashed line shows the osmotic pressure profile along the process. Because the area underneath the blue solid line is larger than the red one in Figure 1(a), the difference, or the shaded area, represents the energy saving of RO-2 relative to RO-1. When the number of stages increases, the shaded area becomes larger, indicating more energy saving, as shown in Figure 1(b). One shortcoming of such a diagram is, however, that the system permeation flux may not be constant when the shaded area becomes larger. While the energy advantage of the two-stage seawater RO (SWRO) over the one-stage counterpart is a well-known fact [9, 10], the intrinsic mechanism for its energy saving benefit is not the same as the one shown in Figure 1.

In this work, mass and momentum transport models [11, 12] will be employed to provide an unambiguous explanation of the P-Y diagrams and their implications for energy consumption in RO processes. It is worth noting that SWRO and low-salinity brackish water RO (BWRO) should be treated separately. The difference is originated from the difference in feed osmotic pressures and operating regimes [13]. SWRO has a much higher feed concentration (typically 35 g/L) than low-salinity BWRO (about 1 g/L based on most municipal RO plants in Southern California). The osmotic pressures are about 27 bar and 0.6 bar, respectively. As a result, the applied pressure is about 60 bar in SWRO and only 15 bar in low-salinity BWRO. The pressure

drop (1-2 bar per pressure vessel housing 6 to 8 elements connected in series) to the feed osmotic pressure ratio is small in SWRO but very large in BWRO. Often times, the friction loss in BWRO outweighs the osmotic pressure on the energy consumption [14]. Moreover, SWRO is operated near the thermodynamic limit, whereas the applied pressure in BWRO is far above the osmotic pressure [13]. As a result, more details may be required for mathematical modeling and P-Y diagram construction for BWRO than SWRO.

2. Modeling

2.1. RO with high-salinity feed

Consider a SWRO in which the primary resistance to permeation is the osmotic pressure. As a first approximation, the effect of concentration polarization, retentate pressure drop, and salt passage is ignored. It is also assumed that the permeate is at atmospheric pressure. As a result, the water flux (J_w) is described by the Darcy's law in the following form:

$$J_{w} = -\frac{dQ}{dA}$$

$$= L_{p}(\Delta P - \Delta \pi)$$

$$= L_{p}(P - \pi)$$
(1)

where -dQ is the flow rate of water across the membrane of area dA, L_p is the membrane hydraulic permeability, P and π are the hydraulic pressure and osmotic pressure, respectively, and Δ represents transmembrane properties. If the applied pressure and the feed rate are given, an integration of Equation (1) will yield the retentate rate at the outlet of this RO stage.

For an N-stage SWRO with interstage booster pumps and an energy recovery device (ERD) with 100% efficiency, the theoretical specific energy consumption (SEC) normalized by the feed osmotic pressure (π_0), or NSEC

(a dimensionless quantity), is [15]:

$$NSEC = \frac{SEC}{\pi_0}$$

$$= \frac{Q_0 P_0 + \sum_{j=1}^{N-1} Q_j (P_j - P_{j-1}) - Q_N P_{N-1}}{Y Q_0 \pi_0}$$

$$= \frac{1}{Y} \sum_{j=0}^{N-1} \frac{P_j}{\pi_0} \frac{(Q_j - Q_{j+1})}{Q_0}$$
(2)

where P_j and Q_j are the pressure and volumetric flow rate at the entrance of stage j + 1. Y is the overall system recovery. The subscript 0 represents inlet conditions.

An optimization model has been developed to minimize the theoretical NSEC (Equation (2)) subject to the transport law (Equation (1)) in each stage [11]. To have a comparison on the same footing, the intake flow (Q_0) , total membrane area (A_m) , membrane permeability (L_p) and recovery (Y) are all fixed [11]. Under such conditions, the non-dimensional design parameter γ (defined as $A_m L_p \pi_0/Q_0$) and the design flux \bar{J}_w (defined as $Q_0 Y/A_m$) are both constant. The optimization program optimally allocates membrane areas and permeate productions among the stages and determines the best applied pressure in each stage. It is noted that modern SWRO plants have a γ in the ballpark of 0.8 [13] and a recovery of 30-50% [16]. Additionally, they are equipped with ERDs whose efficiency is close to 100% [17].

The spatial profiles of P/π_0 (solid lines), π/π_0 (dashed lines), and $J_w/(L_p\pi_0)$ in single-stage RO and multi-stage ROs with interstage booster pumps at Y = 50% solved by the optimization program are shown in Figure 2. Two values of γ (1 and 2) are used for the study. When more permeable membranes become available in the market, the γ parameter in SWRO is expected to increase. At a fixed γ , the osmotic pressures in all cases start and end at the same values, even though they each takes a different spatial path. The applied pressures, however, have completely different trends from the osmotic pressures. As the number of stage increases, the applied pressure is lowered in the first stage but elevated in the last stage. In such a way, the areas bounded by the solid and dashed lines in all RO configurations in Figure

2(a) or (b) are the same. In fact, this can be verified mathematically,

$$\int_{0}^{1} \left(\frac{P}{\pi_{0}} - \frac{\pi}{\pi_{0}} \right) d\left(\frac{A}{A_{m}} \right) = \frac{\int_{0}^{A_{m}} L_{p}(P - \pi) dA}{A_{m} L_{p} \pi_{0}}$$

$$= \frac{Y}{\gamma} \tag{3}$$

It is observed from Figure 2(c) or (d) that the area underneath each curve is also the same, or

$$\int_{0}^{1} \left(\frac{J_{w}}{L_{p}\pi_{0}} \right) d\left(\frac{A}{A_{m}} \right) = \frac{\int_{0}^{A_{m}} J_{w} dA}{A_{m}L_{p}\pi_{0}}$$

$$= \frac{\bar{J}_{w}}{L_{p}\pi_{0}} \tag{4}$$

where \bar{J}_w is the spatial average flux $(\bar{J}_w = \frac{1}{A_m} \int_0^{A_m} J_w dA)$.

Equations (3) and (4) are equivalent, or $Y/\gamma = Y/(A_m L_p \pi_0/Q_0) = \bar{J}_w/(L_p \pi_0)$. This implies that the bounded area between the applied pressure and the osmotic pressure in Figure 2(a) or (b) is essentially the dimensionless average flux $\bar{J}_w/(L_p \pi_0)$.

From Figure 2(c) or (d), the spatial variation in flux gradually reduces as the number of stages increases. As N becomes infinity, the permeation flux is spatially uniform [15]. In such a case, it is equivalent to an ideal batch RO, whose flux is temporally invariant [15].

When γ increases from 1 to 2, the dimensionless spatial-average flux is halved (based on the identity $\bar{J}_w/(L_p\pi_0)=Y/\gamma$), and the applied pressure moves closer to the osmotic pressure. For RO-1, the rear end of the membrane may contribute very little to permeate production. This implies that the system is approaching the thermodynamic limit [18, 19]. A further increase in γ using the one-stage design may not offer differentiable energy saving benefit, exhibiting "the law of diminishing returns" in the NSEC- γ curve [20]. However, when the design configuration changes from single-stage to two-stage with an interstage booster pump, permeate production at the end of the RO is ameliorated. As γ further increases, the horizontal asymptote may be approached again, and changing the RO configuration to three-stage with two interstage booster pumps can further enhance the flux uniformity

and lower the NSEC [11]. This illustrates the trade-off between kinetics and energetics in SWRO [21].

It is seen from Figure 2(a) or (b) that the spatial profile of osmotic pressure is lowered generally as the number of stages increases, implying less salt transport across the membrane if its salt rejection is imperfect. Moreover, increasing the membrane permeability while keeping all other parameters except the applied pressure the same may lower the permeate quality, which can be mitigated by using multistage design with interstage booster pumps.

The relative spatial uniformity of flux in Figure 2 can also been seen in the Y-A diagram shown in Figure 3. A greater than 1 slope at a particular location implies a higher-than-average flux and vice versa. Moreover, the gap between each curve and the 45 degree identity line reflects the degree of non-uniformity. Apparently, as γ increases, the spatial variation in flux becomes greater, and more RO stages and interstage booster pumps would be required to achieve the same level of uniformity.

Additionally, a point on the curve that is above the diagonal line in Figure 3 means that the cumulative production up to this location is above the system average. It is seen that the transition points between different stages sit very close to the diagonal line, implying that the stage-average fluxes are very close in each multi-stage RO. In other words, the permeation production in each stage is approximately proportional to the membrane area allocated to it under optimal conditions.

The pressures can also be plotted as functions of percentage of completion (or cumulative recovery y divided by its final value Y), as shown in Figure 4. If there is no pressure drop in the retentate channel, the area underneath of each solid curve in the P-Y diagram is essentially the NSEC, which may be shown by the equation below:

$$NSEC = \frac{1}{Y} \sum_{j=0}^{N-1} \frac{P_j}{\pi_0} \frac{(Q_j - Q_{j+1})}{Q_0}$$

$$= \frac{1}{Y} \int_0^Y \frac{P}{\pi_0} dy$$

$$= \int_0^1 \frac{P}{\pi_0} d\left(\frac{y}{Y}\right)$$
(5)

where $Q_j - Q_{j+1}$ is the permeate production in stage j+1 and $\sum_{j=0}^{N-1} \frac{Q_j - Q_{j+1}}{Q_0} =$

Y.

The area underneath the dashed curve in Figure 4 $(\pi/\pi_0 = 1/(1-y))$ is the minimum NSEC imposed by thermodynamics:

$$NSEC_{Thermo} = \int_{0}^{1} \frac{1}{1-y} d\left(\frac{y}{Y}\right)$$
$$= -\frac{1}{Y} \ln(1-Y)$$
 (6)

The area bounded by each pair of the solid and dash curves in Figure 4 represents the extra energy requirement to maintain the system design flux (\bar{J}_w) , or

$$NSEC_{Flux} = \int_0^1 \left(\frac{P}{\pi_0} - \frac{1}{1 - y}\right) d\left(\frac{y}{Y}\right) \tag{7}$$

 $NSEC_{Flux}$ is different for different RO configurations, even if \bar{J}_w is kept constant. For example, when $\gamma=1$ and Y=50%, the bounded areas in Figure 4(a) calculated using trapezoidal numerical integration are 0.69, 0.54, 0.52, and 0.50 for RO-1, RO-2, RO-3, and RO- ∞ , respectively. When γ becomes 2, the bounded areas in Figure 4(b) are 0.62, 0.33, 0.29, and 0.25, respectively. In the ideal case where the flux is spatially uniform, $NSEC_{Flux}$ reaches its minimum $(\bar{J}_w/(L_p\pi_0))$ or Y/γ .

To prove this mathematically, define $f_1 = \frac{P}{\pi_0} - \frac{1}{1-y}$ and $f_2 = \frac{d(y/Y)}{d(A/A_m)}$. It can be verified that $\frac{f_1}{f_2} = \frac{\bar{J}_w}{L_p\pi_0}$, $\int_0^1 f_1 d\left(\frac{A}{A_m}\right) = \frac{\bar{J}_w}{L_p\pi_0}$, and $\int_0^1 f_2 d\left(\frac{A}{A_m}\right) = 1$. Now define g_1 and g_2 as the deviations of f_1 and f_2 from their respective averages, or $g_1 = f_1 - \frac{\bar{J}_w}{L_p\pi_0} = (f_2 - 1)\frac{\bar{J}_w}{L_p\pi_0}$ and $g_2 = f_2 - 1$, then $\int_0^1 g_1 d\left(\frac{A}{A_m}\right) = 0$, and $\int_0^1 g_2 d\left(\frac{A}{A_m}\right) = 0$. In addition, $g_1g_2 = (f_2 - 1)^2 \frac{\bar{J}_w}{L_p\pi_0} \ge 0$. Therefore,

$$NSEC_{Flux} = \int_0^1 \left(\frac{P}{\pi_0} - \frac{1}{1 - y}\right) d\left(\frac{y}{Y}\right)$$

$$= \int_0^1 (f_1 f_2) d\left(\frac{A}{A_m}\right)$$

$$= \int_0^1 \left(g_1 + \frac{\bar{J}_w}{L_p \pi_0}\right) (g_2 + 1) d\left(\frac{A}{A_m}\right)$$

$$= \int_0^1 (g_1 g_2) d\left(\frac{A}{A_m}\right) + \frac{\bar{J}_w}{L_p \pi_0}$$

$$= \left[1 + \int_0^1 (f_2 - 1)^2 d\left(\frac{A}{A_m}\right)\right] \frac{\bar{J}_w}{L_p \pi_0}$$

$$(8)$$

It is seen that $NSEC_{Flux} \geq \frac{\bar{J}_w}{L_p \pi_0}$. The equal sign holds only if $f_2 \equiv$

1, which implies $\frac{d(y/Y)}{d(A/A_m)} \equiv 1$, or alternatively, $J_w \equiv \bar{J}_w$. The term

$$\left[\int_0^1 \left(\frac{d(y/Y)}{d(A/A_m)} - 1 \right)^2 d\left(\frac{A}{A_m} \right) \right]$$
 is the penalization coefficient on the mini-

mum NSEC imposed by the system design flux $(\bar{J}_w/(L_p\pi_0))$ due to variation in flux. For single-stage design operated at Y=50%, it is 38% if $\gamma=1$ and 148% if $\gamma=2$. It reduces to 8% and 32%, respectively, by adopting two-stage design with the optimal interstage booster pressure.

A comparison between two different RO configurations can be made using shaded areas, as shown in Figure 5. Different from Figure 1, the shaded areas in Figure 5 are always in pairs. If they are numbered numerically from the left to the right (i.e. $S_1, S_2, ...$), the difference in NSEC between two design configurations can be calculated by the sum of differences in each pair. For example, the NSEC saving of RO-2 relative to RO-1 in Figure 5(a) is (S_1-S_2) . This also applies to the difference between RO- ∞ and RO-1 in Figure 5(e). The energy saving of RO-3 relative to RO-2 in Figure 5(c), however, should be calculated by $(S_1 - S_2) + (S_3 - S_4)$. While the difference between RO-1 and RO-2 is readily seen from Figure 5, it is not so apparent between RO-2 and RO-3. Detailed numerical calculations show that RO-3 is only slightly better than RO-2.

As γ increases from 1 to 2, there is more room for energy saving by upgrading the design configuration from RO-1 to RO-2. This implies that

multi-stage SWRO will likely be more attractive despite the increased system complexity when ultra-permeable SWRO membranes become available [22]. Interestingly, if γ is arbitrarily reduced to 0.2, there is barely any difference in energy performance between single- and multi-stage configurations for SWRO [15]. In such a case, the applied pressure sits much higher than the osmotic pressure in the P-A diagram, and the Y-A curves are closer to the diagonal line.

It is found that P/π_0 vs A/A_m in Figure 2 and P/π_0 vs y/Y in Figure 4 are almost identical, due to the nearly indistinguishable stage-average fluxes in each multi-stage configuration explained previously. Figures 2 and 4 confirm that the system design flux in Figure 1 used in literature is not a constant when the applied pressure is moved closer to the osmotic pressure.

The above observations are substantiated by the equipartition of entropy production theorem [23], which states that separation processes are enhanced by distributing as evenly as possible a function of entropy production along the space and time variables of the process. To put it in another way, the variance of the distribution of driving forces should be minimized to maximize process performance.

Recently, closed-circuit RO (CCRO) [14, 24, 25, 26] and other variants (batch RO [27, 28, 29] and improved CCRO [30, 31]) have been studied. In CCRO, a time-dependent pressure is applied to a closed-circuit where the retentate is recycled back to the RO inlet and the membrane is periodically flushed so that the flitration and flushing steps can be repeated from cycle to cycle. Batch RO and improved CCRO avoid the undesired mixing between the fresh feed and the recycle stream by installing a volume-varying cylinder in front of the CCRO. Optimal control theory has been applied to CCRO and batch RO (or improved CCRO) to determine the best temporal trajectory of applied pressure in the filtration step [15, 32]. It was found out that the flux should be time-invariant in order for NSEC to be minimized, consistent with the equipartition of entropy production theorem. The temporal profiles of pressures and fluxes using the same design parameters (i.e. Y = 50% and $\gamma = 1, 2$) in one CC filtration period $(0 - t_{FT})$ are presented in Figure 6. The definition of γ here is the same as the one in conventional RO, or $\gamma = Y L_p \pi_0 / J_w$. Because the flux is temporally invariant, t/t_{FT} is essentially the same as y/Y. In such a case, the P-t diagram is the same as the P-Y diagram. Obviously, the batch RO (or the improved CCRO) always outperforms the CCRO, and the difference is illustrated by the shaded area in Figure 6. Moreover, the former should also have a better permeate quality

in that the temporal osmotic pressure sits lower.

Similar to the continuous single- and multi-stage RO systems, the area underneath each dashed curve represents the minimum energy imposed by thermodynamics. For the batch RO and the improved CCRO, it is the same as Equation (6). For the original CCRO, however, it is greater (1+Y/2)/(1-Y)) [32, 33]. This is due to the undesired entropy generation induced by mixing of two streams of different concentrations. On the one hand, the internal staging feature of CCRO reduces energy consumption by improving flux uniformity. On the other hand, the undesirable mixing of retentate and fresh feed streams in CCRO adds to energy consumption. The superimposed effect of both factors leads to comparable energy performance of CCRO and RO-1 for $\gamma = 1$ and Y = 50% if ERD is used in both cases. The CCtype designs (CCRO, batch RO, and improved CCRO) have energy saving advantages at a large γ , for example, when ultra-permeable membranes are widely adopted in SWRO. Note that salt retention is a detrimental issue in all CC-type designs, which will give rise to extra energy consumption [32]. These cyclic designs may be combined with the use of novel spacers to enhance mass transfer coefficient for suppressing concentration polarization at high flux conditions and to improve membrane flushing efficacy before the next CC filtration cycle [34, 35, 36, 37].

The above analysis suggests that under fixed intake flow, membrane area and recovery conditions, the following relationship holds:

Peak pressure (or final pressure in each cycle) in CCRO = peak pressure in BRO and improved CCRO > last stage pressure in multi-stage RO > applied pressure in single-stage RO.

It is worth pointing out membrane compaction and embossing at elevated pressures [38] may have a negative impact on performance of CC-type ROs and multi-stage ROs.

2.2. RO with low-salinity feed

For low-salinity BWRO, Equation (1) is coupled with the following pressure drop equation:

$$-\frac{dP}{dL} = 2f\frac{1}{D_H}\rho \left(\frac{Q}{N_{PV}A_c}\right)^2 \tag{9}$$

where dL is the differential length along the RO feed channel, f is the Fanning friction coefficient, D_H is the hydraulic diameter of the spacer-filled feed

channel, ρ is the density of the fluid, N_{PV} is the number of pressure vessels in parallel, and A_c is the cross-sectional area of the feed channel in each RO element. The constant parameters in Equation (9) may be grouped into one single term which is then determined from regression of plant data [12].

A RO train from the Chino I plant is chosen for this study. It employs a two-stage configuration (28:14 array, each pressure vessel housing 7 FilmTec BW30-400 elements) to achieve an 81% recovery. There is no booster pump between the two stages, or the hydraulic pressure reduces continuously along the RO feed channel. It is worth pointing out that the general guideline for BWRO design is one stage for 40–60% recovery, two stages for 70–80% recovery, and three stages for 85–90% recovery, which is to avoid exceeding the maximum single-element recovery (about 15% in municipal plants). The feed rate and osmotic pressure are 1525 gpm (346.4 m³/hr) and 9 psi (0.62 bar), respectively. The membrane permeability L_p is 0.11 gfd/psi (2.74 lmh/bar). The γ parameter is calculated to be 0.053, much smaller than the one in SWRO. Mathematical models have been developed and validated in a wide range of experimental conditions in the plant [12, 39, 40].

In this study, three cases (no interstage booster pump, interstage pump with low boost pressure, and interstage pump with high boost pressure) are considered. The ratio of the boost pressure to the first stage inlet pressure in each case is 0, 0.1 and 0.3, respectively. To account for advances in the field of ultrapermeable membranes, each of the three cases also considers a hypothetical scenario where the membrane permeability is doubled. Equations (1) and (9) are solved simultaneously to determine the flow and pressure conditions in each stage so that the target recovery (81%) is achieved based on the same feed and membrane conditions. The spatial profiles of pressure and flux in each case are shown in Figure 7. It is observed that the use of interstage pumps may improve spatial flux uniformity and permeate quality as well. When the membrane permeability is doubled, the applied pressure is lowered closer to the osmotic pressure. Notably, the dimensionless flux $(J_w/(L_p\pi_0)=Y/\gamma)$ in low-salinity BWRO is much higher than that in SWRO. As a result, the improvement in flux uniformity is very limited. The Y-A curves are close to the diagonal line, as shown in Figure 8, differing from those in the SWRO cases presented in Figure 3. Additionally, as the water production in the second stage increases to reduce variation in flux, the spatial flow profile is elevated (Figures 8(c) and (d)), implying more friction loss.

The P-Y diagram based on current plant operating conditions is shown

in Figure 9(a). Using trapezoidal numerical integration, the areas bounded by the solid and dashed curves are calculated to be 15.6, 15.5, and 15.4 for no boost, low boost and high boost, respectively. Apparently, the NSEC imposed by system design flux does reduce slightly as the spatial uniformity of flux improves, which is consistent with Equation 8. In the hypothetical ideal case where there is no spatial variation in flux, it is $\bar{J}_w/(L_p\pi_0) = Y/\gamma = 15.3$. If no booster pump is used, the penalization coefficient on the minimum NSEC imposed by system flux due to spatial flux variation is only 2\%. In the hypothetical cases where the membrane permeability is twice that of the FilmTec BW30-400 membrane, the areas bounded by the solid and dashed curves in Figure 9(b) are 8.3, 8.1, and 7.9 for no boost, low boost and high boost, respectively. The penalization coefficient due to flux non-uniformity is 9%, 6% and 3%, respectively. The NSEC dictated by osmotic pressure is $-\ln(1-Y)/Y=2.1$, which is much smaller than the NSEC imposed by system flux. In other words, the operation is far above the thermodynamic limit.

Figure 9(a) or (b) cannot be directly used to interpret the total energy consumption in BWRO because of significant pressure drop and no ERD. In such a case, Equation (2) must be modified:

$$NSEC = \frac{Q_0 P_0 + \sum_{j=1}^{N-1} Q_j (P_j - P_{j-1} + P_{d_j})}{Y Q_0 \pi_0}$$

$$= \frac{Q_0 P_0 + \sum_{j=1}^{N-1} Q_j (P_j - P_{j-1} + P_{d_j}) - Q_N (P_{N-1} - P_{d_N}) + Q_N (P_{N-1} - P_{d_N})}{Y Q_0 \pi_0}$$

$$= \frac{1}{Y} \sum_{j=0}^{N-1} \frac{P_j}{\pi_0} \frac{Q_j - Q_{j+1}}{Q_0} + \frac{1}{Y} \sum_{j=1}^{N} \frac{P_{d_j}}{\pi_0} \frac{Q_j}{Q_0} + \frac{1}{Y} \frac{P_{N-1} - P_{d_N}}{\pi_0} \frac{Q_N}{Q_0}$$

$$= \frac{1}{Y} \sum_{j=0}^{N-1} \left(\frac{P_j}{\pi_0} + \frac{P_{d_{j+1}}}{\pi_0} \frac{Q_{j+1}}{Q_j - Q_{j+1}} \right) \frac{Q_j - Q_{j+1}}{Q_0} + \frac{1}{Y} \frac{P_{N-1} - P_{d_N}}{\pi_0} \frac{Q_N}{Q_0}$$
(10)

where P_j and Q_j are the pressure and volumetric flow rate at the entrance of stage j + 1, defined the same as in Equation (2). P_{d_j} is the pressure drop

in stage j. Note that $\frac{Q_{j+1}}{Q_j - Q_{j+1}}$ is the retentate to permeate ratio in stage j+1 and that $\sum_{j=0}^{N-1} \frac{Q_j - Q_{j+1}}{Q_0} = Y$.

The first term on the R.H.S. of Equation (10) represents the NSEC required for overcoming osmotic pressure and friction loss and satisfying the flux requirement (or the NSEC with the use of an ERD), and the second term describes the brine energy dissipated by the brine valve.

The NSEC calculated using Equation (10) is 24.7, 25.0 and 25.7 for no boost, low boost and high boost, respectively (or 15.2, 15.3 and 15.7 if the membrane permeability is doubled). This trend is opposite to the one in the previous case in which only osmotic pressure and flux are taken into consideration. To illustrate the effect of flow resistance, the P-Y diagram is reconstructed and shown in Figures 9(c) and (d). The height of each horizontal segment is $\left(\frac{P_j}{\pi_0} + \frac{P_{d_{j+1}}}{\pi_0} \frac{Q_{j+1}}{Q_j - Q_{j+1}}\right)$ (j = 0 and 1). Therefore, the area underneath each dash-dotted line represents the first term on the R.H.S. of Equation (10). The area bounded by each pair of dash-dotted and solid curves stands for the effect of friction loss. Apparently, it is even greater than the area underneath the osmotic pressure curve.

To further demonstrate the trend, the ratio of the interstage boost pressure to the first stage inlet pressure is varied in the range of 0-0.5 while maintaining the same system recovery rate. As this ratio increases, the first stage pressure is lowered and the second stage pressure is elevated, resulting in a gradual shift of permeate production to the second stage. As a consequence, the spatial uniformity of flux improves initially, reaching the most balanced condition at a ratio of 0.24 (or 0.39 if the permeability is doubled), then deteriorates. The standard deviation of flux (based on 20 uniformly distributed intervals in the first stage and 10 uniformly distributed intervals in the second stage) and the corresponding NSEC required by design flux calculated from Equation (7) are shown in Figures 10(a) and (b). Apparently, the spatial uniformity of flux is directly correlated to the NSEC required by the system design flux, and this trend obeys Equation 8 and the equipartition of entropy production theorem. However, the total NSEC calculated from Equation (10) is a monotonic function of the boost/first-stage pressure ratio, as shown in Figure 10(b). The total NSEC is further broken down by osmotic pressure (calculated by Equation (6)), design flux (calculated by Equation (7)), brine energy not recovered (calculated by the last term on the R.H.S. of Equation (10)), and friction loss (calculated by the first term on the R.H.S. of Equation (10) subtracted by Equations (6) and (7)). The increased NSEC with the boost/first-stage pressure ratio in Figure 10(b) is attributed to increased friction loss and brine energy dissipated via the brine valve. In addition, only a very small portion of the energy is used to overcome the osmotic pressure in low-salinity BWRO. These are very different from SWRO.

It is worth pointing out that even though an interstage booster pump is not used at the Chino I Desalter, it is popular in BWRO plants which offers benefits including balanced flux, improved permeate quality, reduced fouling in the first stage, extended membrane life, and ability to control permeate flow in individual stage. However, it may come with an extra energy cost in addition to capital investment.

If salt retention or pressure drop is not taken into consideration, the P-Y diagram for CC-type designs applied to BWRO is similar to Figure 6, except that the constant gap between the applied pressure and the osmotic pressure (or $J_w/(L_p\pi_0)$) is much wider. Moreover, the shaded area in Figure 6 increases rapidly as the recovery goes beyond 90%, highlighting the superior energy performance of the improved CCRO over the original CCRO for ultrahigh recovery applications [30, 31]. The P-Y diagram alone does not reveal the overall energy consumption in CC-type ROs because many technical details (e.g. friction loss, salt retention, membrane flushing efficacy and others) are not considered. In such a case, detailed numerical simulations become important [14, 30, 31]. For example, at a recovery of 95% and a feed TDS of 1 g/L, CCRO may consume 30% more energy than batch RO, improved CCRO and multi-stage RO, provided that the operation is not limited by scaling [31]. The trend is consistent with a recent experimental study [29].

Similar to the use of interstage booster pumps in multi-stage RO, the internal staging feature in CC-type designs for low-salinity BWRO applications can only slightly reduce energy consumption required by design flux. If only one RO element is used in CC-type systems, the typical single-pass recovery is about 10% (which is why an industrial BWRO plant operated at 90% recovery requires at least 3 stages, or 21 elements in series if each pressure vessel has 7 elements). This implies that the recirculation flow is 9 times of the fresh feed. Even though the pressure drop across one RO element in CC-type systems is small (about 0.2 bar), the recirculation pump still consumes a fair amount of energy because of the high flow rate. More-

over, CC-type ROs in small-scale applications often suffer from low pump efficiencies due to small pump sizes, and therefore, the actual SEC in CC-type ROs in small-scale BWRO applications may be even higher than that in large-scale continuous multi-stage plants.

The conclusions on substantial energy saving benefit of CC-type ROs relative to continuous multi-stage ROs for ultrahigh recovery low-salinity BWRO applications in literature may be attributed to unmatched conditions. For example, using smaller flow rates and higher single-pass recoveries (e.g. 25% or greater for one single RO element which is atypical in industrial design) will nullify the effect of friction. Additionally, using a more permeable membrane and/or a smaller system design flux will also reduce the energy consumption (because of a larger γ). Nevertheless, the CC-type designs offer beneficial features such as time-invariant flow, small footprint, operational flexibility, and relative resistance to fouling and scaling, which have been discussed in literature at length.

3. Conclusions

The construction of P-Y diagrams usually requires a mathematical model. The area underneath the P-Y curve represents the NSEC imposed by design flux and thermodynamics, which may be reduced by improving flux uniformity. When there is no variation in flux, it reaches the theoretical minimum, $(\bar{J}_w/(L_p\pi_0) + \ln[1/(1-Y)]/Y$ or $Y/\gamma + \ln[1/(1-Y)]/Y$ for conventional RO, improved CCRO and BRO or $\bar{J}_w/(L_p\pi_0) + Y/[2(1-Y)]$ or $Y/\gamma + Y/[2(1-Y)]$ for CCRO). The trend follows the equipartition of entropy production theorem in literature.

The P-Y diagram can reasonably describe the overall NSEC in SWRO since the pressure drop to feed osmotic pressure ratio is small and the operation is near the thermodynamic limit. The staged design in conjunction with interstage booster pumps enable a more uniform flux, thus reducing the NSEC.

The P-Y diagram is not sufficient to reveal the overall NSEC in low-salinity BWRO due to significant friction losses relative to the feed osmotic pressure as well as operation far above the thermodynamic limit. Improving flux uniformity may lead to a higher energy consumption if the increased friction loss exceeds the reduced energy imposed by system design flux.

The use of ultrapermeable membranes may reduce the minimal NSEC imposed by the design flux $(\bar{J}_w/(L_p\pi_0))$. However, the spatial flux variation

will be greater, and the penalization coefficient for the calculation of the actual NSEC required by the design flux $\left(\int_0^1 \left(\frac{d(y/Y)}{d(A/A_m)} - 1 \right)^2 d\left(\frac{A}{A_m} \right) \right]$

will increase. Moreover, more salt transport would occur in light of imperfect membranes. Both can be compensated by adding interstage booster pumps or optimizing booster pump pressures. Based on cases studied in this work, doubling membrane permeability in SWRO and switching from one-stage to two-stage with an interstage booster pump would reduce the SEC by 17%. For low-salinity BWRO, doubling the membrane permeability may reduce the SEC by about 40%.

From a viewpoint of SEC, the original CCRO is a thermodynamically inferior design, especially at high recoveries. Its internal staging feature is advantageous for reducing SEC when γ is large.

Acknowledgement

The authors would like to acknowledge financial support from the National Alliance for Water Innovation (NAWI), funded by the US Department of Energy, Office of Energy Efficiency and Renewable Energy (EERE), Advanced Manufacturing Office, under Funding Opportunity Announcement Number DE-FOA-0001905. Mingheng Li would also like to thank the National Science Foundation (CBET-2140946). Any opinions, findings, conclusions, or recommendations expressed in this material are those of the authors and do not necessarily reflect the views of the funders.

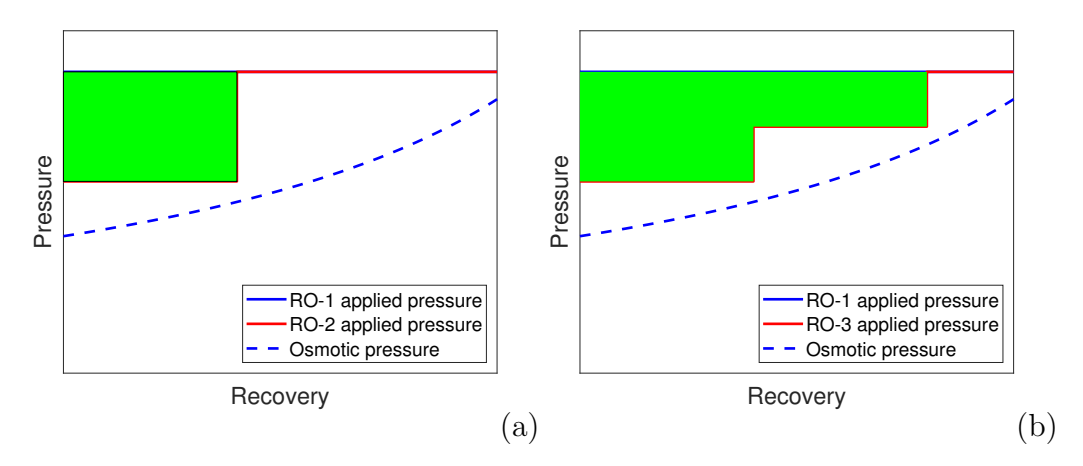


Figure 1: An example of using shaded area to represent energy saving in the P-Y diagram. (a) RO-1 and RO-2. (b) RO-1 and RO-3.

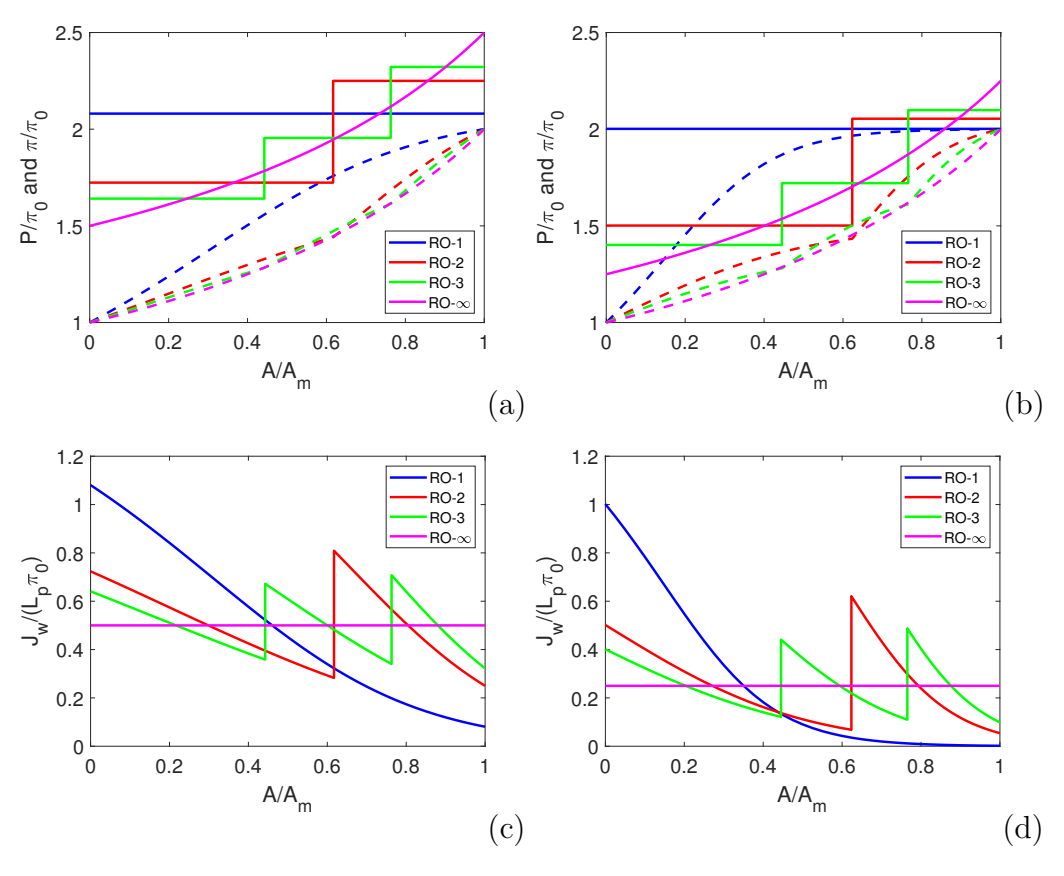


Figure 2: Spatial profiles of (a,b) P/π_0 (solid lines) and π/π_0 (dashed lines), and (c,d) $J_w/(L_p\pi_0)$ in single- and multi-stage SWROs. Y=50%. (a,c) $\gamma=1$ and (b,d) $\gamma=2$. Effect of concentration polarization and friction loss is not included.

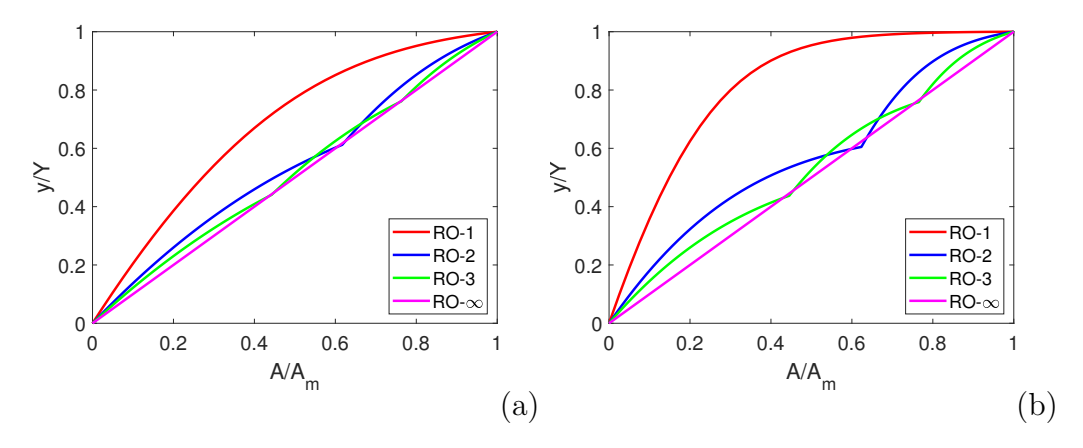


Figure 3: Y-A diagram showing relative flux uniformity in single- and multi-stage SWROs. Y=50%. (a) $\gamma=1$ and (b) $\gamma=2$. Effect of concentration polarization and friction loss is not included.

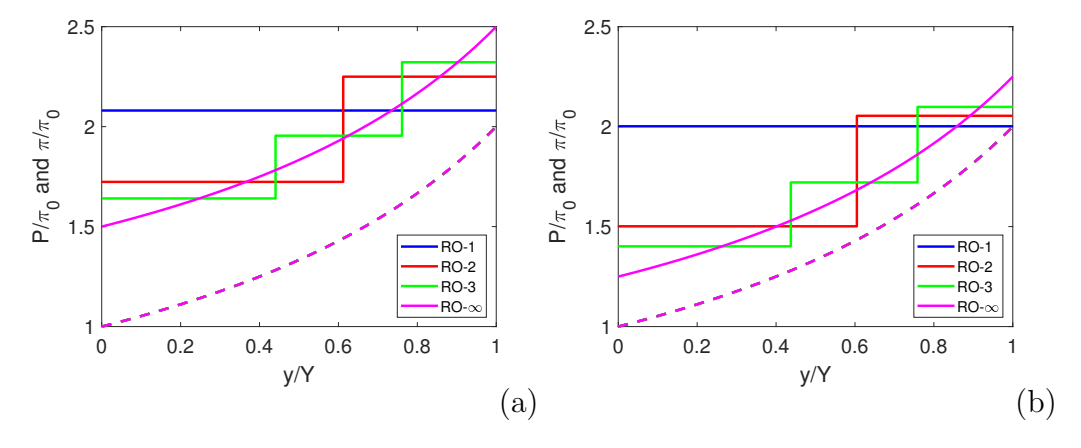


Figure 4: P/π_0 (solid lines) and π/π_0 (dashed lines) in single- and multi-stage SWROs in the P-Y diagram. Y=50%. (a) $\gamma=1$ and (b) $\gamma=2$. Effect of concentration polarization and friction loss is not included.

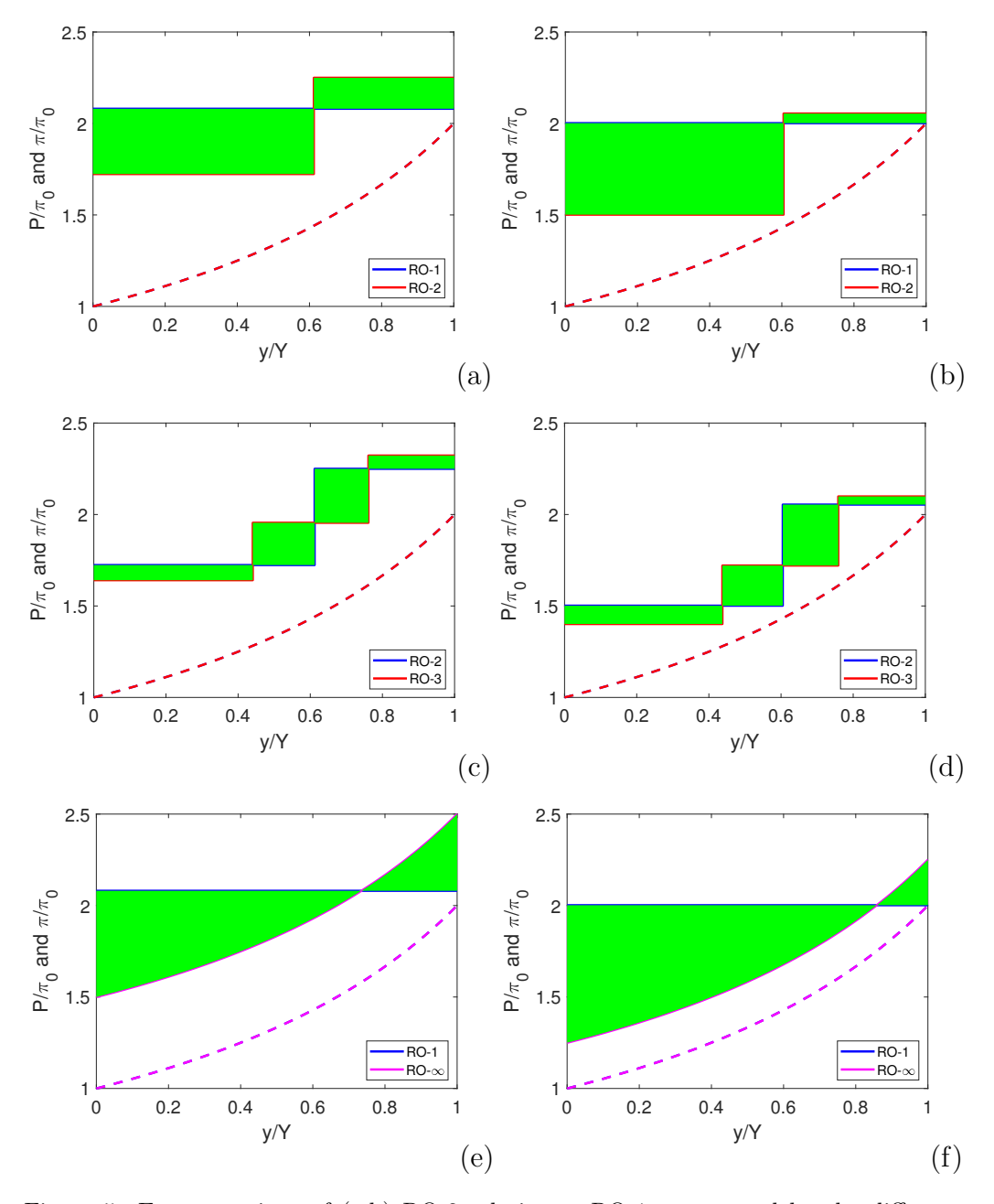


Figure 5: Energy savings of (a,b) RO-2 relative to RO-1 represented by the difference between one pair of shaded areas, (c,d) RO-3 relative to RO-2 represented by the added sum of the differences of two pairs of shaded areas, and (e,f) RO- ∞ relative to RO-1 represented by the difference between one pair of shaded areas. Y=50%. (a,c,e) $\gamma=1$ and (b,d,f) $\gamma=2$. Effect of concentration polarization and friction loss is not included.

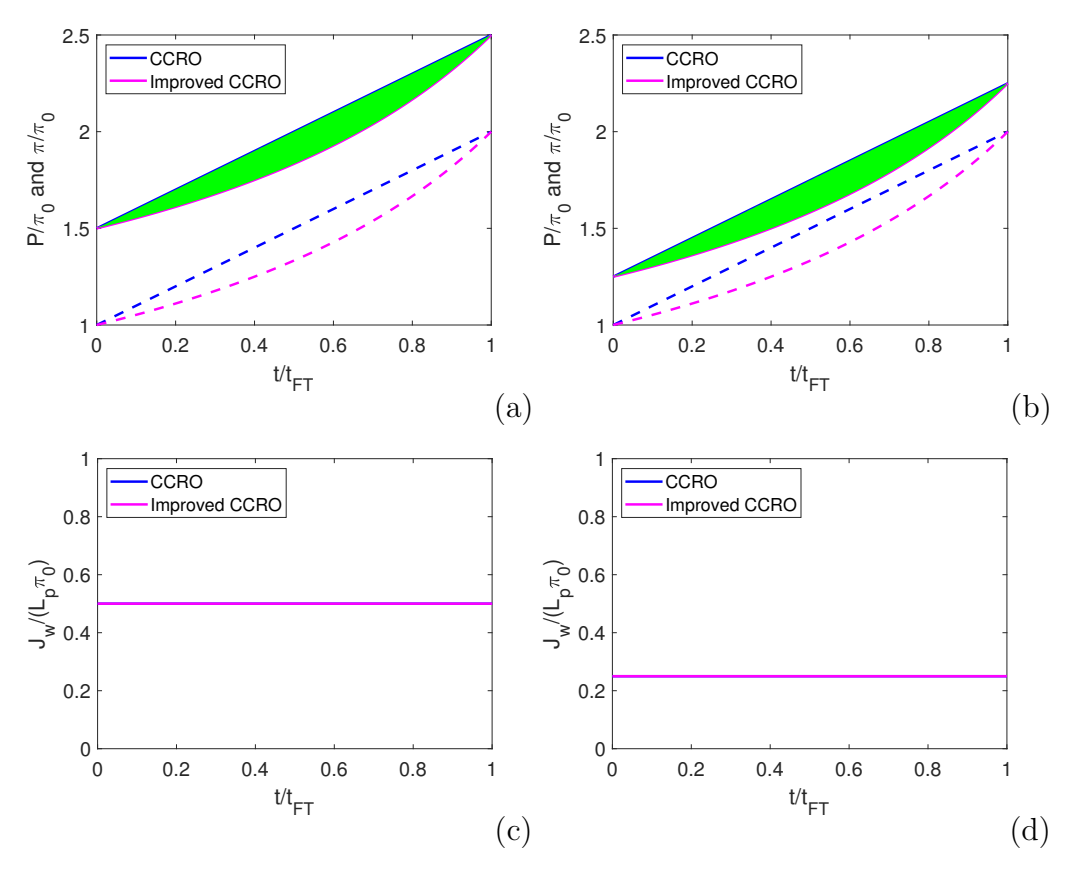


Figure 6: Temporal profiles of (a) P/π_0 (solid lines) and π/π_0 (dashed lines), and (b) spatial average $J_w/(L_p\pi_0)$ in CCRO and improved CCRO. Y=50%. (a,c) $\gamma=1$ and (b,d) $\gamma=2$. Effect of concentration polarization, friction loss, and cycle-to-cycle salt buildup is ignored.

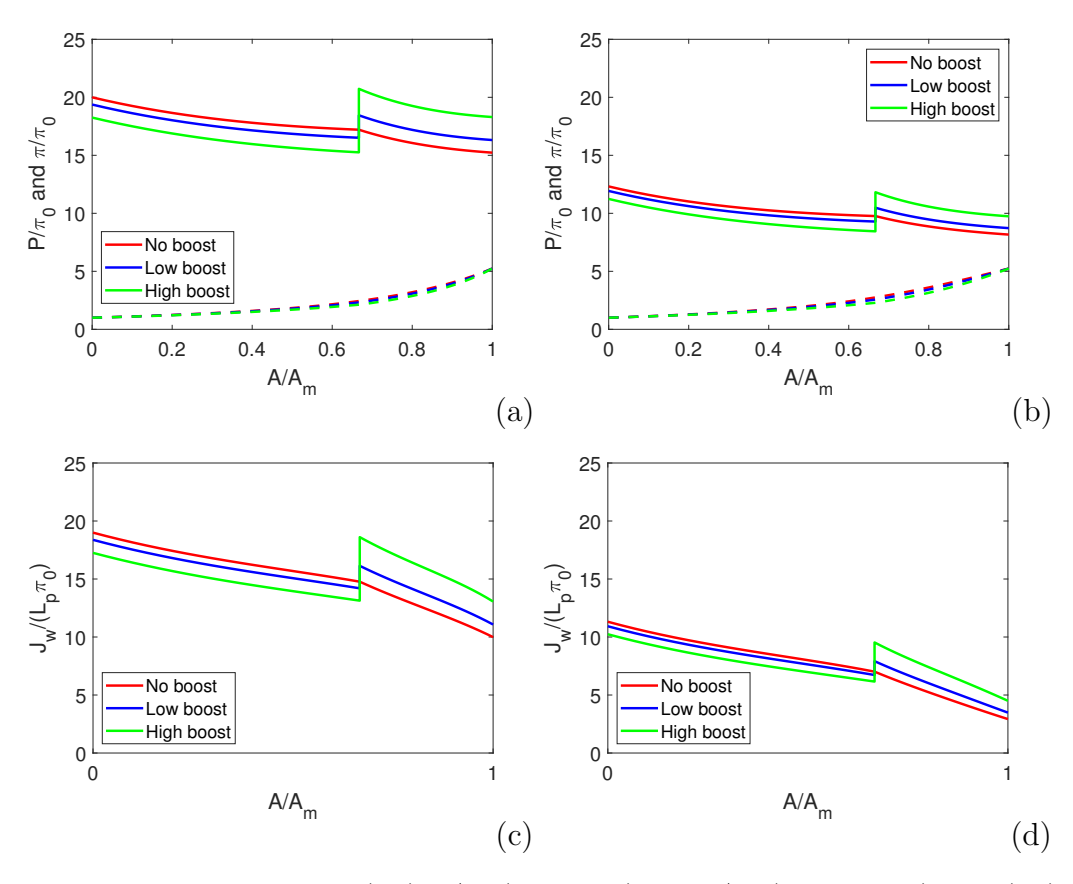


Figure 7: Spatial profiles of (a,b) P/π_0 (solid lines) and π/π_0 (dashed lines), and (c,d) $J_w/(L_p\pi_0)$ in a two-stage BWRO. Y=81%. (a,c) $\gamma=0.053$. (b,d) $\gamma=0.106$ (by doubling L_p).

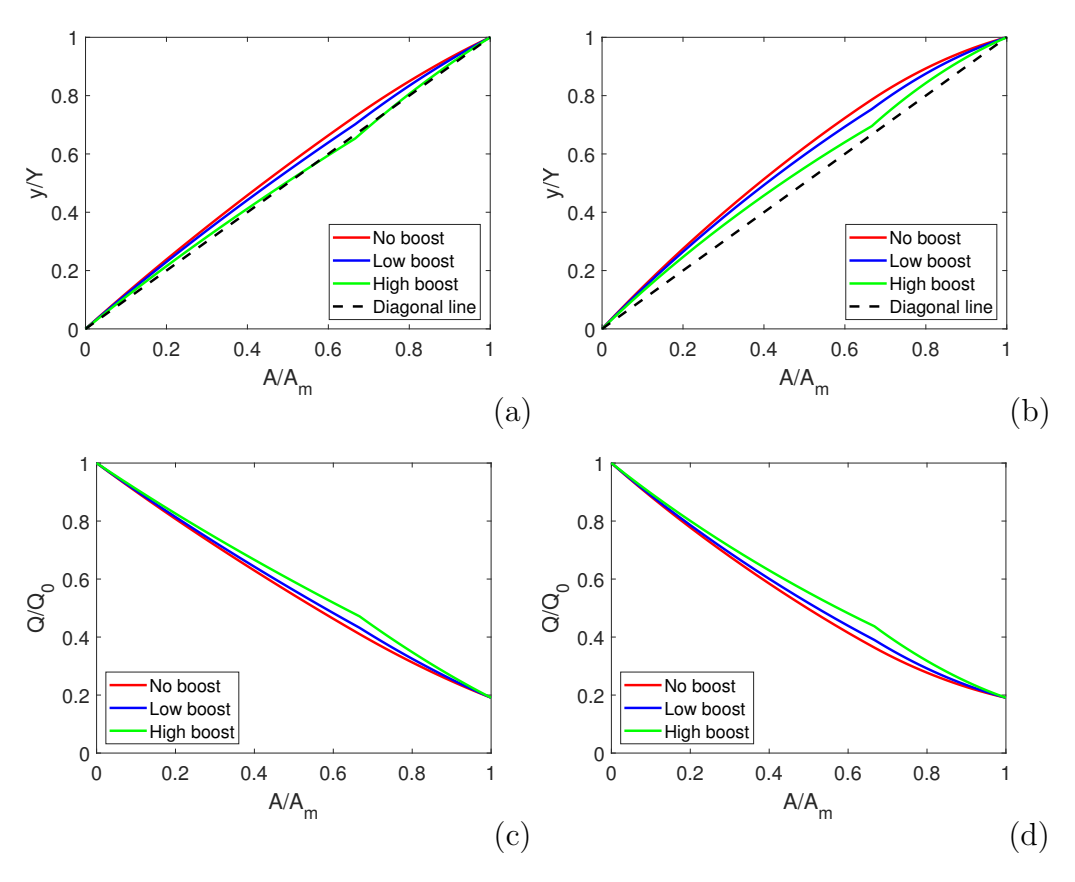


Figure 8: (a,b) Y-A diagram and (c,d) Q-A diagram showing relative flux uniformity in a two-stage BWRO. Y = 81%. (a,c) $\gamma = 0.053$. (b,d) $\gamma = 0.106$ (by doubling L_p).

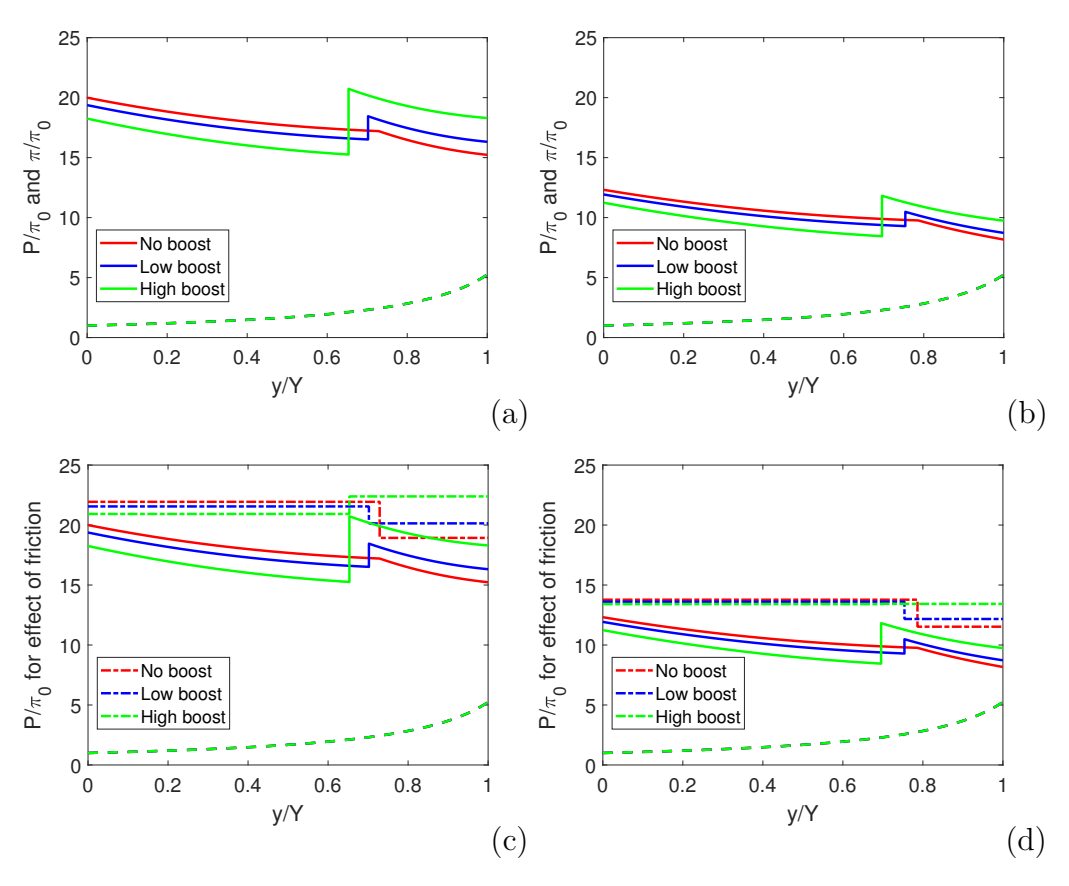


Figure 9: (a,b) P/π_0 (solid lines) and π/π_0 (dashed lines) in a two-stage BWRO in the P-Y diagram. (c,d) reconstructed P-Y diagram showing the effect of friction loss by the area bounded by solid and dash-dotted lines. Y=81%. (a,c) $\gamma=0.053$. (b,d) $\gamma=0.106$ (by doubling L_p).

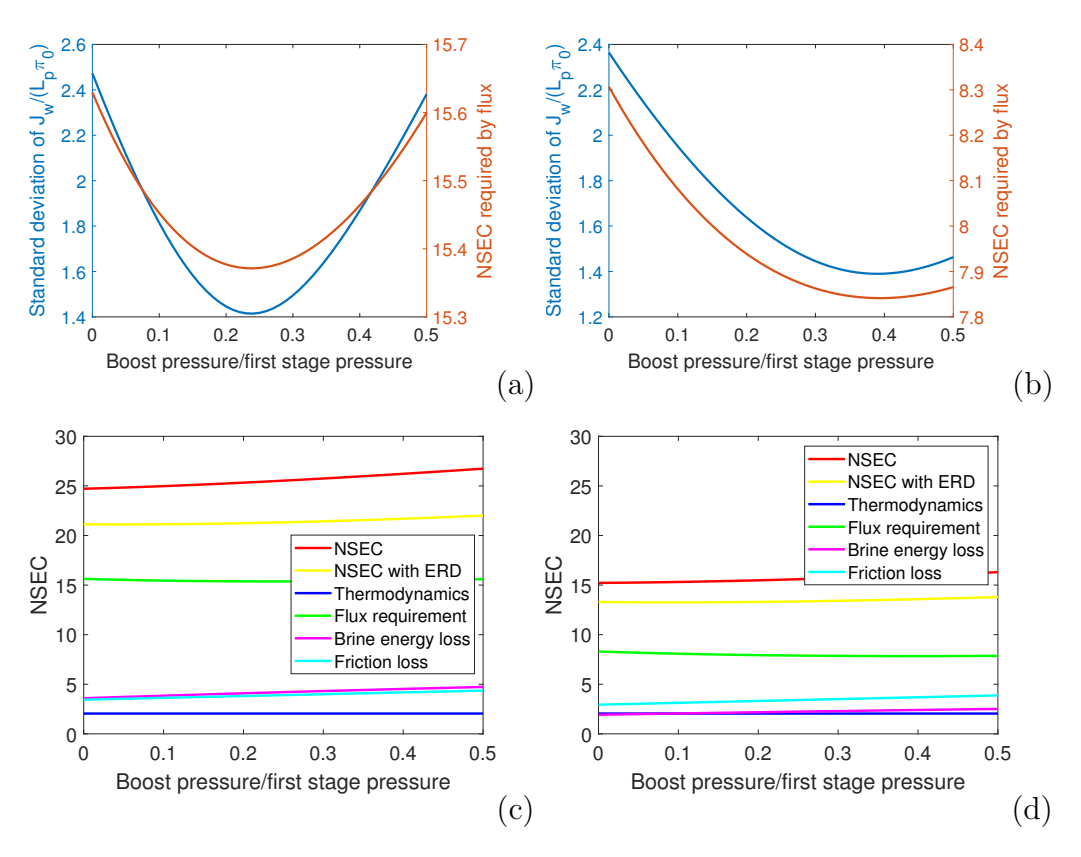


Figure 10: (a,b) Standard deviation of spatial flux and NSEC required by flux, (b,d) breakdown analysis of NSEC as a function of the boost pressure to first stage pressure ratio. Y=81%. (a,c) $\gamma=0.053$. (b,d) $\gamma=0.106$ (by doubling L_p).

References

- [1] M. J. Moran, H. N. Shapiro, D. D. Boettner, M. B. Bailey, Fundamentals of Engineering Thermodynamics, 9th Edition, Wiley, 2020.
- [2] C. Liu, K. Rainwater, L. Song, Energy analysis and efficiency assessment of reverse osmosis desalination process, Desalination 276 (2011) 352–358.
- [3] M. Elimelech, W. A. Phillip, The future of seawater desalination: energy, technology, and the environment, Science 333 (6043) (2011) 712–717.
- [4] R. L. Stover, High recovery, low fouling, and low energy reverse osmosis, Desalin. Water Treat. 57 (2016) 26501–26506.
- [5] X. Chen, N. Y. Yip, Unlocking high-salinity desalination with cascading osmotically mediated reverse osmosis: energy and operating pressure analysis, Environ. Sci. Technol. 52 (2018) 2242–2250.
- [6] Q. J. Wei, C. I. Tucker, P. J. Wu, A. M. Trueworthy, E. W. Tow, J. H. Lienhard V, Impact of salt retention on true batch reverse osmosis energy consumption: Experiments and model validation, Desalination 479 (2020) 114177.
- [7] K. Park, P. A. Davies, A compact hybrid batch/semi-batch reverse osmosis (hbsro) system for high-recovery, low-energy desalination, Desalination 504 (2021) 114976.
- [8] H. E. Elsayed-Ali, Elevation-distributed multistage reverse osmosis desalination with seawater pumped storage, Appl. Water Sci. 13 (2023) 48.
- [9] M. Taniguchi, M. Kurihara, S. Kimura, Behavior of a reverse osmosis plant adopting a brine conversion two-stage process and its computer simulation, J. Membr. Sci. 183 (2001) 249–257.
- [10] Y. Kim, Y.-G. Park, K. Park, Optimal design strategy, heuristics, and theoretical analysis of multi-stage reverse osmosis for seawater desalination, Desalination 580 (2024) 117534.
- [11] M. Li, Reducing specific energy consumption in reverse osmosis (RO) water desalination: An analysis from first principles, Desalination 276 (2011) 128–135.

- [12] M. Li, Optimal plant operation of brackish water reverse osmosis (BWRO) desalination, Desalination 293 (2012) 61–68.
- [13] M. Li, A unified model-based analysis and optimization of specific energy consumption in BWRO and SWRO, Ind. Eng. Chem. Res. 52 (2013) 17241–17248.
- [14] M. Li, Cyclic simulation and energy assessment of closed-circuit RO (CCRO) of brackish water, Desalination 545 (2023) 116149.
- [15] M. Li, Dynamic operation of batch reverse osmosis and batch pressure retarded osmosis, Ind. Eng. Chem. Res. 59 (2020) 3097–3108.
- [16] B. A. Sharkh, A. A. Al-Amoudi, M. Farooque, C. M. Fellows, S. Ihm, S. Lee, S. Li, N. Voutchkov, Seawater desalination concentrate—a new frontier for sustainable mining of valuable minerals, npj Clean Water 5 (2022) 9.
- [17] R. L. Stover, Seawater reverse osmosis with isobaric energy recovery devices, Desalination 203 (2007) 168–175.
- [18] L. Song, J. Y. Hu, S. L. Ong, W. J. Ng, M. Elimelech, M. Wilf, Emergence of thermodynamic restriction and its implications for full-scale reverse osmosis processes, Desalination 155 (2003) 213–228.
- [19] A. Zhu, P. D. Christofides, Y. Cohen, Effect of thermodynamic restriction on energy cost optimization of RO membrane water desalination, Ind. Eng. Chem. Res. 48 (2009) 6010–6021.
- [20] M. Li, Minimization of energy in reverse osmosis water desalination using constrained nonlinear optimization, Ind. Eng. Chem. Res. 49 (2010) 1822–1831.
- [21] S. Lin, M. Elimelech, Kinetics and energetics trade-off in reverse osmosis desalination with different configurations, Desalination 401 (2017) 42–52.
- [22] J. Luo, M. Li, E. C. Hoek, Y. Heng, Supercomputing and machine learning-aided optimal design of high-permeability seawater reverse osmosis membrane systems, Sci. Bull. 68 (2023) 397–407.

- [23] D. Tondeur, E. Kvaalen, Equipartition of entropy production. an optimality criterion for transfer and separation processes, Ind. Eng. Chem. Res. 26 (1987) 50–56.
- [24] D. M. Warsinger, E. W. Tow, K. G. Nayar, L. A. Maswadeh, J. H. Lienhard V, Energy efficiency of batch and semi-batch (CCRO) reverse osmosis desalination, Water Res. 106 (2016) 272–282.
- [25] T. Lee, A. Rahardianto, Y. Cohen, Multi-cycle operation of semi-batch reverse osmosis (SBRO) desalination, J. Membr. Sci. 588 (2019) 117090.
- [26] H. Gu, M. H. Plumlee, M. Boyd, M. Hwang, J. C. Lozier, Operational optimization of closed-circuit reverse osmosis (CCRO) pilot to recover concentrate at an advanced water purification facility for potable reuse, Desalination 518 (2021) 115300.
- [27] E. Hosseinipour, K. Park, L. Burlace, T. Naughton, P. A. Davies, A free-piston batch reverse osmosis (RO) system for brackish water desalination: Experimental study and model validation, Desalination 527 (2022) 115524.
- [28] E. Hosseinipour, E. Harris, H. A. El Nazer, Y. M. Mohamed, P. A. Davies, Desalination by batch reverse osmosis (RO) of brackish ground-water containing sparingly soluble salts, Desalination 566 (2023) 116875.
- [29] E. Hosseinipour, P. Davies, Direct experimental comparison of batch reverse osmosis (RO) technologies, Desalination (2024) 117717.
- [30] M. Li, An improved closed-circuit RO (CCRO) system: Design and cyclic simulation, Desalination 554 (2023) 116519.
- [31] M. Li, Effect of cylinder sizing on performance of improved closed-circuit RO (CCRO), Desalination 561 (2023) 116688.
- [32] M. Li, Effects of finite flux and flushing efficacy on specific energy consumption in semi-batch and batch reverse osmosis processes, Desalination 496 (2020) 114646.
- [33] S. Lin, M. Elimelech, Staged reverse osmosis operation: Configurations, energy efficiency, and application potential, Desalination 366 (2015) 9–14.

- [34] W. Lin, J. Lei, Q. Wang, X. Wang, X. Huang, Performance enhancement of spiral-wound reverse osmosis membrane elements with novel diagonal-flow feed channels, Desalination 523 (2022) 115447.
- [35] Y. K. Chong, Y. Y. Liang, G. A. Fimbres-Weihs, Validation and characterisation of mass transfer of 3D-CFD model for twisted feed spacer, Desalination 554 (2023) 116516.
- [36] J. Luo, M. Li, Y. Heng, Bio-inspired design of next-generation ultrapermeable membrane systems, npj Clean Water 7 (2024) 4.
- [37] Q. Yang, J. Luo, M. Li, S. Lin, Inverse design of v-shape feed spacer for batch and semi-batch reverse osmosis, Desalination (in press 2024).
- [38] J. Wu, B. Jung, A. Anvari, S. Im, M. Anderson, X. Zheng, D. Jassby, R. B. Kaner, D. Dlamini, A. Edalat, E. M. V. Hoek, Reverse osmosis membrane compaction and embossing at ultra-high pressure operation, Desalination 537 (2022) 115875.
- [39] M. Li, B. Noh, Validation of model-based optimization of brackish water reverse osmosis (BWRO) plant operation, Desalination 304 (2012) 20–24.
- [40] M. Li, T. Bui, S. Chao, Three-dimensional CFD analysis of hydrodynamics and concentration polarization in an industrial RO feed channel, Desalination 397 (2016) 194–204.